Journal of Materials Chemistry A

ROYAL SOCIETY OF CHEMISTRY

PAPER

View Article Online
View Journal | View Issue

Cite this: *J. Mater. Chem. A*, 2025, **13**, 35267

Covalent grafting of redox-active sites onto MXenes with spinel ACo_2O_4 (A = Zn, Cu) integration for tailored interfacial charge storage in high-performance supercapacitors

Jitesh Pani* and Hitesh Borkar *

Received 14th July 2025
Accepted 21st August 2025

DOI: 10.1039/d5ta05685c

rsc.li/materials-a

The urgent demand for efficient energy storage underscores the importance of chemically tunable nanomaterials. MXenes, with their adjustable surface groups and metallic conductivity, are ideal for supercapacitor electrodes. In this work, redox-active sulphonate groups were covalently grafted onto $Ti_3C_2T_x$ MXene *via* a simple DMSO-assisted grinding method. Further enhancement was achieved by integrating 15 wt% of spinel $ZnCo_2O_4$ (15ZTS) and $CuCo_2O_4$ (15CTS), resulting in specific capacitances of 564.11 and 543.38 F g^{-1}, respectively, with excellent cycling stabilities (84.75% and 78.49% after 10 000 cycles). A symmetric supercapacitor using 15ZTS demonstrated real-world applicability by powering LEDs and retained 65.6% capacitance after 5000 cycles. The device delivered energy and power densities of 6.45 Wh kg^{-1} and 598.48 W kg^{-1}. Theoretical studies confirmed that sulphonate functionalisation and oxide integration significantly modulate the electron environment, enhancing charge storage. This strategy offers a scalable pathway toward high-performance, redox-active MXene-based supercapacitors for next-generation energy storage applications.

1. Introduction

Global energy consumption is intensifying at a rapid pace and continues to rely on fossil fuels, a trend closely associated with population expansion and heightened energy needs. The existing energy production and distribution systems lack the capacity to adequately address the accelerating global demand for energy.[1] Renewable energy sources possess immense potential, but their intermittency, high initial installation cost, environmental effects and limited availability underscore the critical need for robust and efficient energy storage systems like supercapacitors and batteries, which hold promise for future applications.[2] The increase in electric vehicles and wearable electronics has demanded high power and energy density storage devices. Conventionally, batteries function by harnessing energy from redox reactions occurring between their active materials and the electrolyte, achieving high energy density but facing challenges such as reduced cycle life and limited power output. Supercapacitors, also referred to as ultracapacitors, integrate the advantages of high-power density and energy density, effectively bridging the functional gap between batteries and traditional capacitors. A battery shows high energy density but poor power density whereas a supercapacitor shows higher power density and energy density making it a suitable device for pulse power driven applications.[3] Supercapacitors are classified into two categories based on their charge storage mechanisms: Electrostatic Double-Layer Capacitors (EDLCs) and pseudo capacitors.[4] EDLCs utilize the adsorption and desorption of ionic species to create an electrostatic double layer, enabling fast charging, discharging, and remarkable stability.[5] The electrode materials include graphene, carbon nanotubes, and activated carbon. In contrast, the charge storage mechanism of pseudo-capacitors is driven by fast and reversible redox reactions occurring at the interface between the electrode and electrolyte, enabling higher storage than double-layer capacitors (materials-such as polymers, transition metal dichalcogenides (TMDs), and MXenes). Although supercapacitors have reduced gravimetric or volumetric energy storage in comparison to batteries, integrating hybrid chemistries of surface dominated and redox dominated charge storage, has emerged as an effective method to enhance their performance.[6]

Choosing a material and the electrolyte is crucial for optimising supercapacitor performance and making it promising for industrial scale production while keeping the production process hazard free and commercially feasible.[7] In this aspect, materials like TMDs, layered double hydroxides (LHDs), metal organic frameworks and carbon-based materials have been explored extensively.[8–13]

Nowadays, MXenes, a member of the 2D materials, have gained attention of scientific researchers owing to their layered

Department of Physics, National Institute of Technology, Warangal, Telangana 506004, India. E-mail: jp712165@student.nitw.ac.in; bhitesh@nitw.ac.in

conductive sheets, ease of preparation, and hydrophilic nature in an electrolyte medium.[14] The hydrophilic nature and the higher mechanical stability of layered sheets of MXenes make them excellent candidates for higher stability electrode materials. Owing to these properties MXenes are now being explored in diverse domains such as fuel cells, sensors, actuators, triboelectric nanogenerators (TENGs), solar cells and electrochemical energy storage devices.[15–20] Despite their advantageous properties, MXene nanosheets exhibit restacking behaviour, predominantly determined by interlayer van der Waals forces.[21] Restricted electrolyte ion accessibility resulting from layer restacking impedes optimum utilization of MXene's active sites. Secondly, functional groups like oxides and fluorides present on the surface of MXene materials may exhibit unstable reactions with the electrolyte, resulting in surface degradation during prolonged use and affecting cycling stability.[22] MXene restacking and surface deterioration can be addressed through introducing electrolyte ion-reactive sites through functionalization and incorporating intercalation nanomaterials within its conductive sheets.

Diverse strategies like ball milling, self-assembly, sonication, hydrothermal processes, and chemical methods, have been employed to functionalize MXenes with small molecules, macromolecules, and individual heteroatoms.[23] The sulphonation of MXene sheets has been implemented in this work as the chosen functionalization technique to amplify redox-active sites for electrochemical storage dominated by faradaic reduction–oxidation processes. The application of arenediazonium salts for MXene surface sulphonation has been validated in earlier studies as a proficient method for methylene blue removal.[24] Nanomaterial surface functionalization, *via* covalent or non-covalent strategies, alters properties for diverse applications including energy storage and biomedicine. Covalent techniques like silanization, thiol–gold binding, and click reactions yield strong bonds that influence electronic behaviour.[25] Non-covalent functionalization methods such as π–π stacking and hydrogen bonding maintain the structural integrity of nanomaterials and are widely employed in graphene and carbon nanotube systems for energy and biomedical applications.[26]

The sulphonation of MXene sheets in the current study was achieved using dimethyl sulphoxide (DMSO), applied *via* a cost-efficient grinding technique. The introduction of DMSO into the MXene layered structure causes an expansion of interlayer spacing, weakening van der Waals force and easing the exfoliation process. DMSO readily forms bonds with terminal functional groups (–OH, –F, and –O), enhancing the exfoliation process. Since DMSO is a polar aprotic solvent, the exfoliated MXene sheets preserve the high electrical conductivity and structural integrity.[27] For improved redox-based charge storage, H_2SO_4 has been used as the electrolyte, with its molarity set at 0.1 M to prioritize safety and adaptability for practical implementation.

Preventing the restacking of MXene nanosheets and the elevation in charge storage efficiency can be achieved by constructing highly conductive three-dimensional (3D) porous architectures. This can facilitate rapid ion diffusion and elevate electrochemical efficiency.[28] The formation of titanium dioxide (TiO_2), caused by the surface oxidation of $Ti_3C_2T_x$ MXene, reduces its conductivity. Incorporating metal oxides or perovskites passivates the surface, preserving conductivity and enhancing electrochemical application performance.[29] Out of several materials to integrate with MXenes, perovskite oxides promise to be excellent candidates for nanocomposite preparation.

Several perovskite oxides with ABO_3, AB_2O_4 (layered or spinel structure), and $A_2B_1B_2O_6$ compositions have been explored for electrochemical studies.[30,31] Spinel perovskite oxides have demonstrated high specific capacitance and energy density due to their favourable electronic structure and abundant redox-active sites. For example, certain AB_2O_4 spinel perovskite oxides exhibit specific capacitances exceeding those of comparable ABO_3 perovskites.[32] The flexibility of choosing A and B site atoms in perovskite oxide makes it more physiochemically accessible for redox ion interaction in electrolyte. Their stable framework and adjustable composition through A- or B-site (in AB_2O_4 spinel perovskite) doping boost electronic conductivity, facilitate extended voltage ranges, and enhance cycling stability surpassing those of numerous traditional transition metal oxides like ZnO, TiO_2, MnO_2 or Fe_3O_4.[33] The intrinsic oxygen vacancies in perovskites and presence of transition metal at tetrahedral or octahedral sites support bulk charge storage beyond surface controlled kinetics and greatly increase capacitance.[34] Electrochemical analysis revealed that perovskite nanoparticles with the smallest B-site transition metal cation, specifically B-cobalt, achieved the highest specific capacitance, which decreased in the order A(Co > Mn > Cr > Fe)O_3. Studies reveal that the choice of B-site cations impacts surface area in perovskite oxides, with these variations directly correlating with changes in their electrochemical properties and supercapacitor efficiency.[35] Cobaltate perovskite oxides (AB_2O_4, where A = Mg, Zn, Co, Cu and B = Co) are distinguished by their superior redox behaviour, electrical performance, and structural stability, making them promising for supercapacitor technologies.[36–39] The exceptional pseudocapacitive performance of these nanomaterials, enabling rapid faradaic processes, is predominantly attributed to the multiple oxidation states of cobalt (Co^{2+}, Co^{3+}, and Co^{4+}).[40]

Perovskite oxides facilitate ion transport through their layered structures, whereas MXenes allow rapid electrolyte infiltration *via* interlayer spacing, and their synergistic effect enhances the electrochemical performance. Oxygen vacancies or dopants in perovskite oxides enhance redox activity, while the adjustable surface terminations of MXenes improve interfacial charge transfer efficiency. The moderate electrical conductivity of perovskite oxides is greatly enhanced by integration with highly conductive MXenes, resulting in an improved electron transport network and superior electrochemical performance. The inherent structural integrity of perovskite oxides combines with the flexibility and mechanical resilience of MXenes to create a robust composite material.

In this work, a cost effective and simple grinding process was undertaken to functionalise the MXene surface with redox active sulphonate ions. The 3D network of $ZnCo_2O_4$ (ZCO) and $CuCo_2O_4$ (CCO) has been integrated with MXenes individually

to enhance the electrochemical performance of MXenes by providing more transport sites and resolving the restacking issue *via* nanoparticle intercalation within the sheets. Zn^{2+} and Cu^{2+} serve as crucial charge carriers in energy storage applications, where their reversible electrochemical properties promote conductivity and increase device stability across several cycles. To understand the integration dynamics, cobaltate perovskite was combined with sulphonated MXene layers through ZCO and CCO formulations at 10, 15, and 20 weight percentage (wt%) proportions. Compared to pure TS, TS integrated with ZCO and CCO exhibited enhanced electrochemical performance, validated through Electrochemical Impedance Spectroscopy (EIS) and Dunn's method calculation. The specific capacitance obtained for 15 wt% ZCO integrated TS (15ZTS) and 15 wt% CCO integrated TS (15CTS) was found to be 564.11 and 543.38 F g^{-1}, respectively, with stabilities of 84.75 and 78.49% after 10 000 cycles. Besides, a lab scale fabricated symmetric supercapacitor (SS) device using redox active 15ZTS demonstrated a specific capacitance of 129.12 F g^{-1} at 2 A g^{-1} current density. The device was tested by using a glowing array of LEDs and it showed 65.6% specific capacitance after 5000 cycles. The power and energy densities are calculated to be 598.48 W kg^{-1} and 6.45 Wh kg^{-1}, respectively. Incorporating theoretical calculations in this study is essential to unravel the underlying atomic-scale interactions that govern the electrochemical behaviour of $Ti_3C_2T_x$ based hybrid systems. While experimental data reflect performance outcomes, theoretical insights interpret the origin of charge redistribution, orbital hybridisation, and electronic conductivity enhancements induced by surface functionalisation and oxide integration. Through density of states, electron density, and effective potential mapping, a clear structure–property correlation is established, which rationalises the superior capacitive performance of the ZTS configuration. The method enables exploration of novel surface treatments for MXenes and fine tuning their electronic properties, which are critical factors for applications such as sensing, energy conversion and storage.

2. Results and discussion

The crystalline phases of all individual (ZCO, CCO, Ti_3AlC_2, $Ti_3C_2T_x$ MXene and TS) prepared materials were confirmed from diffraction patterns, as illustrated in Fig. 1a. The respective compositional phases in TS and Z/CCO are presented in Fig. 1b. The three compositions with 10, 15 and 20 wt% of ZCO in TS were named 10ZTS, 15ZTS and 20ZTS, respectively. Similarly, compositions with 10, 15 and 20 wt% of CCO in TS were named 10CTS, 15CTS and 20CTS, respectively. Changes in Bragg reflections post-etching were distinctly noted in the MXene XRD spectra (Fig. 1a and b). XRD analysis of the pure Ti_3AlC_2 MAX phase displayed a distinct aluminium peak at the (104) plane with a Bragg angle of 38.85°. Following HF etching, the successful etching of Al layer is validated by the absence of the (104) peak in MXene. The XRD diffraction spectra confirm the hexagonal structure of $Ti_3C_2T_x$ MXene (TM) with the $R\bar{3}m$ space group. The diffraction peaks at 8.64°, 18.18°, 27.26°, 34.31° and 60.51° correspond to the (002), (004), (006), (101) and (110) crystal planes of TM, respectively. The diffraction peaks of the MAX phase and TM are consistent with COD card numbers 96-722-1325 and 96-153-2228, respectively. The exfoliation process caused shifts in the (002) plane from 9.37° to 8.64°, the (004) plane from 19.06° to 18.18°, and the (110) plane from 60.64° to 60.51°, attributed to alterations in the *c*-lattice parameter of MAX and TM.[41] The identified *c*-lattice variations are caused by tensile strain. Reduction in crystallite size, as reflected by the broadened peaks, provides additional validation of the nanolayered structural characteristics of TM.[42] The diffraction pattern of TS shows multiple peaks due to grafting of sulphur on the multilayered surface of MXene (Fig. 1b). The sulphonation process resulted in lattice micro strain, as evidenced by the broadening of peaks at the (002) and (110) planes in sulphonated MXene (TS) compared to the pristine TM (Fig. 1a and b).[43] The XRD analysis confirms the formation of ZCO and CCO nanoparticles with a spinel cubic structure having space group $Fd\bar{3}m$, free from secondary phases, matched with COD card numbers 96-591-0137 and 96-591-0156, respectively. The diffraction peaks of ZCO at 18.96°, 31.22°, 36.81°, 38.49°, 44.74°, 55.57°, 59.28°, 65.15° and 77.16° correspond to the (111), (220), (311), (222), (400), (422), (511), (440) and (553) lattice planes, respectively. These peaks of ZCO are consistent with previously reported data.[44] The peaks of CCO at 19.01°, 31.4°, 35.3°, 36.8°, 39°, 44.5°, 55.5°, 59.6° and 65.6° correspond to (111), (220), (311), (222), (400), (422), (511), (440) and (553) lattice planes, respectively, well in agreement with previously reported studies.[45]

FTIR was employed for determining functional groups and chemical bonding in $Ti_3C_2T_x$, TS, ZCO, CCO and 15Z/CTS composites (Fig. 1c). FTIR analysis was conducted utilizing infrared light within the active wavelength range of 500 to 4000 cm^{-1}. This reveals the extent of sulphonation at the MXene surface and the effective integration of ZCO and CCO nanoflowers. The peaks at 3434 and 1628 cm^{-1} of $Ti_3C_2T_x$ MXene correspond to the –OH group anchored to MXene surfaces as a result of the synthesis route.[46] The deformation vibration of Ti–C and Ti–O are observed at 881 and 1025 cm^{-1}.[47] The minor peaks observed at 1645 cm^{-1} correspond to the bending modes associated with H–O–H. The broad peak observed in the range of 3000–3700 cm^{-1} for ZCO and CCO corresponds to the stretching vibrations of O–H bonds on the material surfaces.[48] Peaks at 560 cm^{-1} and 686 cm^{-1} in ZCO correspond to Co–O and Zn–O vibrations, confirming the spinel phase in 15ZTS.[49] Similarly, the peak at 686 cm^{-1} represents the Cu–O bond oscillation in CCO and 15CTS spectra. A reduction in the intensity of the peak corresponding to the –OH group in TS as compared to pristine $Ti_3C_2T_x$ MXene suggests surface sulphonation facilitated by DMSO. A similar reduction of hydroxyl group intensity due to active surface sulphonation can be observed in 15ZTS and 15CTS nanocomposites as compared to the pristine ZCO, CCO and $Ti_3C_2T_x$ MXene.

The characterization of surface area and pore size distribution in pristine TS and its nanocomposites with Z/CCO was completed through BET-BJH analyses. Fig. 1d depicts the N_2 adsorption–desorption isotherms for pristine TS and its composites integrated with cobaltate perovskites ZCO and CCO.

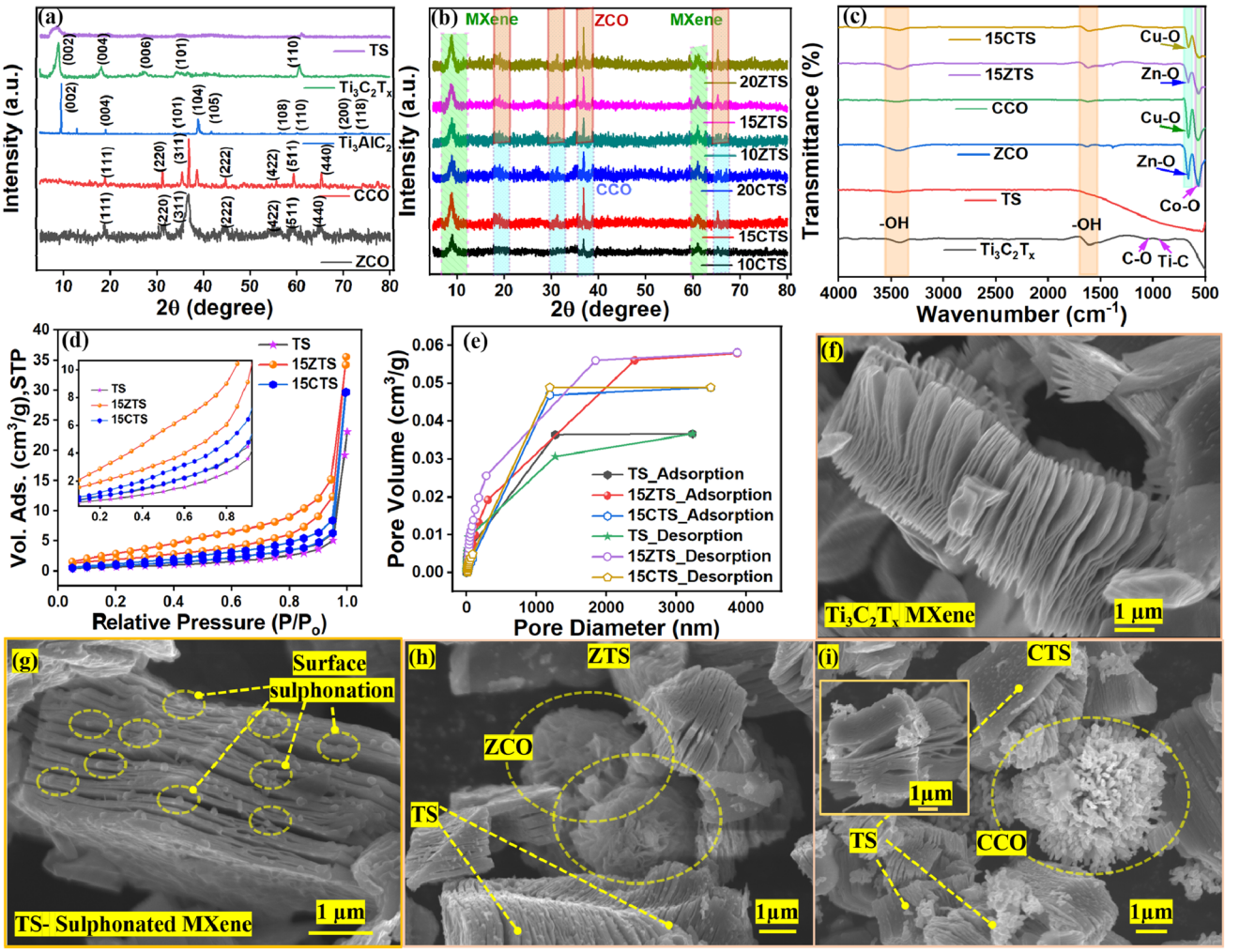

Fig. 1 X-ray diffraction (XRD) pattern of (a) individual materials and (b) composites of TS and Z/CCO, (c) Fourier transform infrared (FTIR) spectra of individual and composite materials, (d) N_2 adsorption–desorption isotherms, (e) pore-volume–distribution curves of TS and 15Z/CTS nanocomposites, and Field Emission Scanning Electron Microscopy (FESEM) images of (f) $Ti_3C_2T_x$ MXene, (g) sulphonated MXene-TS, (h) ZTS composite showing the presence of ZCO with TS and (i) CTS composite showing the presence of ZCO with TS (inset image shows the intercalation of CCO nanoparticles in between the conductive sheets of TS).

The isotherms reveal a stiffer adsorbed volume at a relative pressure of 1, pointing to the multilayer adsorption mechanism between the adsorber (layered sulphonated conductive sheets of MXenes) and adsorbate (N_2). In the lower relative pressure region from 0.1 to 0.9, the increased adsorption sites for adsorbent N_2 indicate the effectiveness in enhancing the adsorption sites of TS by integration and fewer intercalations with ZCO and CCO nanoflowers. In the pristine TS, the observed flat desorption response suggests a reduced evaporation rate, attributed to the entrapment of adsorbates within the slit-like edges of its layered structure. The specific surface areas for TS, 15CTS and 15ZTS were measured to be 2.61, 3.96 and 7.50 m^2 g^{-1}, respectively. The observed enhancement in specific surface area offers a larger active region, facilitating improved ion interactions within the electrolyte medium. Here, more active surface area means more available active sulphonated sites to participate in the redox reaction with H_2SO_4 electrolyte ions. Fig. 1e illustrates the pore size distribution, highlighting an increase in active adsorption sites in the nanocomposites compared to pristine TS. The calculated pore volumes are found to be 0.035, 0.048 and 0.0519 cm^3 g^{-1} in the case of TS, 15CTS and 15ZTS, respectively. The higher pore volume in 15ZTS suggests improved interfacial ion interactions within the electrolyte, leading to greater charge storage capacity, making it a promising candidate for energy storage applications.

Fig. 1f shows the FESEM image of $Ti_3C_2T_x$ MXene and its exfoliated sheets highlight the successful etching process of the Al layer from the Ti_3AlC_2 MAX phase. Fig. 1g shows the sulphonated MXene TS. Surface dots observed on TS are indicative of the functionalization of sulphonate groups at the MXene interface. The uniform grafting of the sulphonate group in TS can be evidenced from elemental analysis provided in SI Fig. S1 and S2. These surface terminated sulphonated sites provide more active sites for electrolyte ion interaction. The integration of ZCO with TS can be evidenced from the representation of the sheet-like structure of ZCO present in TS and ZTS overall

nanocomposite morphology is presented in Fig. 1h. The sheets of ZCO formed under high pressure in an autoclave have formed a nanoflower like structure as evidenced from the morphology. On the other hand, under high-pressure conditions and in the presence of urea, the CCO forms a flower-like morphology. The CCO integrated with TS is shown in Fig. 1i and its presence has been highlighted with circular indications. The intercalation of perovskite nanoparticles into the nanosheets of sulphonated MXene can be confirmed from the details shown in the inset of Fig. 1i. This addresses resolving the restacking issue as well as evolving more active area of TS for electrolyte ion interaction. The active integration of ZCO and CCO with MXene as evidenced can provide its own contribution as well using the conductive root of MXene during electrolyte ion interaction and hence supercapacitor performance in the composites. The agglomeration of nanosheets in the case of ZCO and nanoparticles in the case of CCO for the formation of 3D nanoflowers adds structural stability during the electrolyte rapid ion interaction phase. The detailed colour mapping and the elemental distribution of each individual element in both 15ZTS and 15CTS is provided in SI Fig. S1 and S2.

The surface chemistry, functionalisation, and chemical states of 15ZTS and 15CTS were investigated *via* XPS. The XPS survey spectra of 15ZTS are provided in SI Fig. S3a, indicating the presence of Ti, C, O, Co, Zn and S. Fig. 2a shows the high-resolution survey XPS spectra of Ti 2p. The peaks at 454.8, 458.06 and 458.73 eV correspond to Ti–C, Ti–C–O (Ti $2p_{3/2}$) and TiO_2 (Ti $2p_{3/2}$), respectively. Additionally, peaks at binding energies of 461.48, 463.47 and 464.47 eV correspond to Ti–C–O, Ti_2O_3 (Ti $2p_{1/2}$) and TiO_2 (Ti $2p_{1/2}$), respectively, which align with previously reported results.[50,51] The deconvoluted fitted peaks in the C 1s spectrum (Fig. 2b) indicate Ti–C, C–C, C–O and O–C=O at 280.97, 284.8, 283.99 and 287.92 eV, respectively. The incorporation of the ZCO perovskite material with TS can be confirmed by the presence of Zn, Co and O in 15ZTS as indicated in Fig. 2c–e, respectively. Fig. 2c presents the Zn 2p spectrum with spin–orbit split peaks at (1044.16, 1043.24) and (1021.35, 1020.2) eV, attributed to Zn $2P_{1/2}$ and Zn $2P_{3/2}$, respectively.[52] Fig. 2d shows the XPS spectra for Co 2p. The Co spectrum shows peaks corresponding to Co^{2+} $2p_{1/2}$, satellite Co^{2+} $2p_{1/2}$, Co^{2+} $2p_{3/2}$ and satellite Co^{2+} $2p_{3/2}$, at 794.87, 803.79, 779.55 and 784.04 eV, respectively.[53] The deconvoluted constitutional chemical state of O is shown in Fig. 2e. The peaks at 529.05, 529.63 and 531.09 eV correspond to Ti–O, Ti–O/OH and C–O, respectively. The additional broad spectrum at 531.09 and 529.63 eV also indicated the metal oxide bond Zn–O and Co–O present in 15ZTS.[54] Fig. 2f confirms the successful sulphonate group functionalization by the $SO_4^{2-}/S_2O_3^{2-}$ peak at 167.37 eV.[55] The peaks at 163.1 and 164.98 eV correspond to S $2p_{3/2}$ and S $2p_{1/2}$, respectively.[56] The $SO_4^{2-}/S_2O_3^{2}$ grafted covalently at the surface of MXenes provides an additional redox active site for redox reaction dominated charge storage. The survey spectrum and individual elemental high resolution XPS spectra of 15CTS are provided in SI Fig. S2b–h followed by detailed discussion.

To gain detailed insights into charge storage mechanisms and material behaviour in the composites, the electrochemical measurements were performed using a three electrode setup. In the present work, Cyclic Voltammetry (CV) tests were conducted

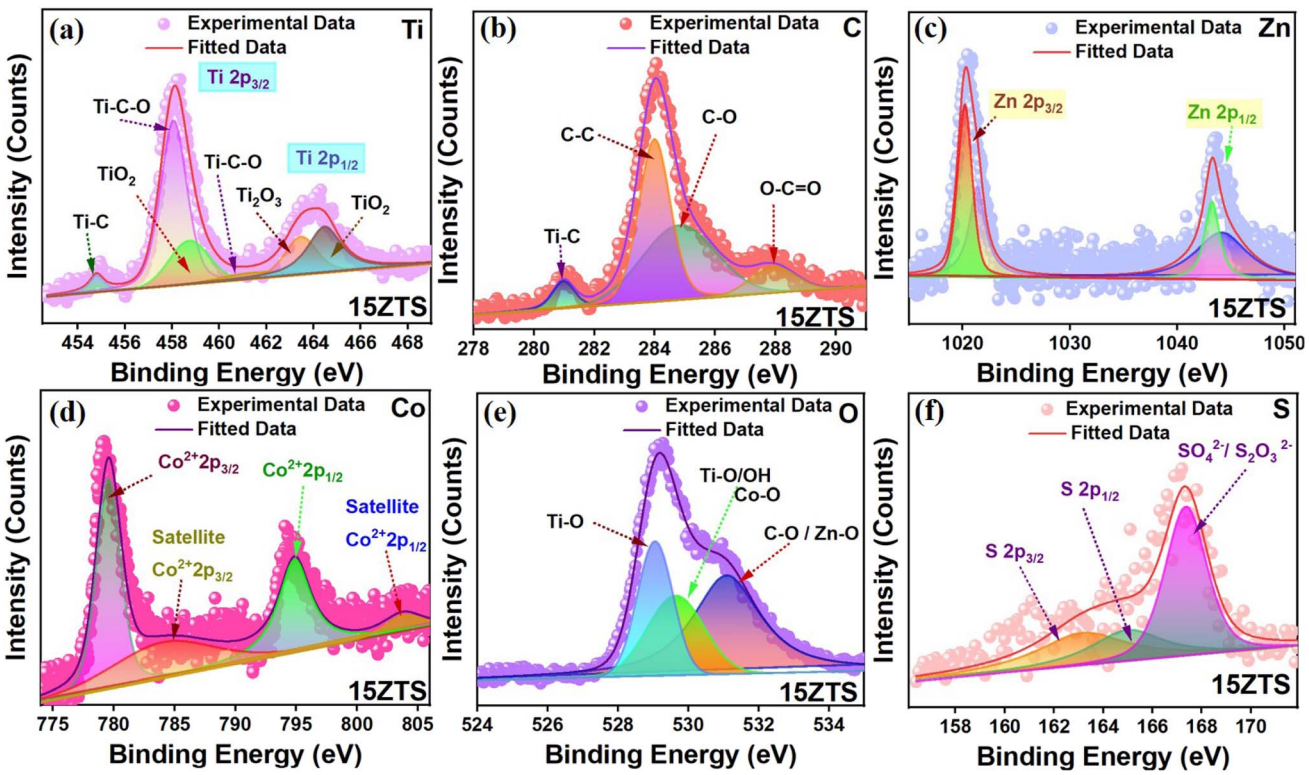

Fig. 2 High resolution XPS spectra for (a) Ti, (b) C, (c) Zn, (d) Co, (e) O and (f) S in 15ZTS.

at scan rates from 5 to 100 mV s^{-1} in the potential window of −0.6 to 0 V. Fig. 3a presents the CV graph derived from the collected CV data, demonstrating the change in current with the applied potential within a particular potential window and exhibiting nearly rectangular and symmetrical patterns. At higher scan rates, the area bound by the curves widens, and the peak current intensifies, highlighting accelerated electronic and ionic transport. This is due to the reversible high-rate faradaic reactions characteristic of pseudocapacitive behaviour. Sharpness of the rectangular profile in the CV graph at elevated scan rates indicates the large redox dominated ion interaction facilitating effective charge redistribution on the electrode surface, leading to improved supercapacitive behaviour. Fig. 3a shows the comparative graph of the CV response of TS, 10, 15, and 20CTS and 10, 15, and 20ZTS at 5 mV s^{-1}. In the present work, the elevated area under the curve of 15ZTS indicates the higher charge storage capabilities, and hence higher specific capacitance. Therefore, the current to voltage response of 15 ZTS at various scan rates from 5 to 100 mV s^{-1} is presented in Fig. 3b. The individual CV curves of TS, alongside the ones for 10 and 20ZTS along with 10, 15, and 20CTS, are presented in SI Fig. S4. The increment in charge interaction and the effective storage can be observed by the synergetic effect of perovskite and MXene sheet integration. The specific capacitance for 15ZTS was calculated to be 564.11 F g^{-1} at 5 mV s^{-1}, whereas for TS and 15CTS, it was 270 and 543 F g^{-1}, respectively. The formulae employed to derive specific capacitance from CV and GCD curves are detailed in the experimental section. The trends of specific capacitance of all the electrodes with respect to the scan rate show uniform charge storing capability even at higher voltage scan rates and are presented in Fig. 3c. Fig. 3d illustrates the galvanostatic charge–discharge behaviour for all samples at a current density of 2 A g^{-1}, revealing prolonged discharge durations in Z/CTS and superior charge storage relative to TS.

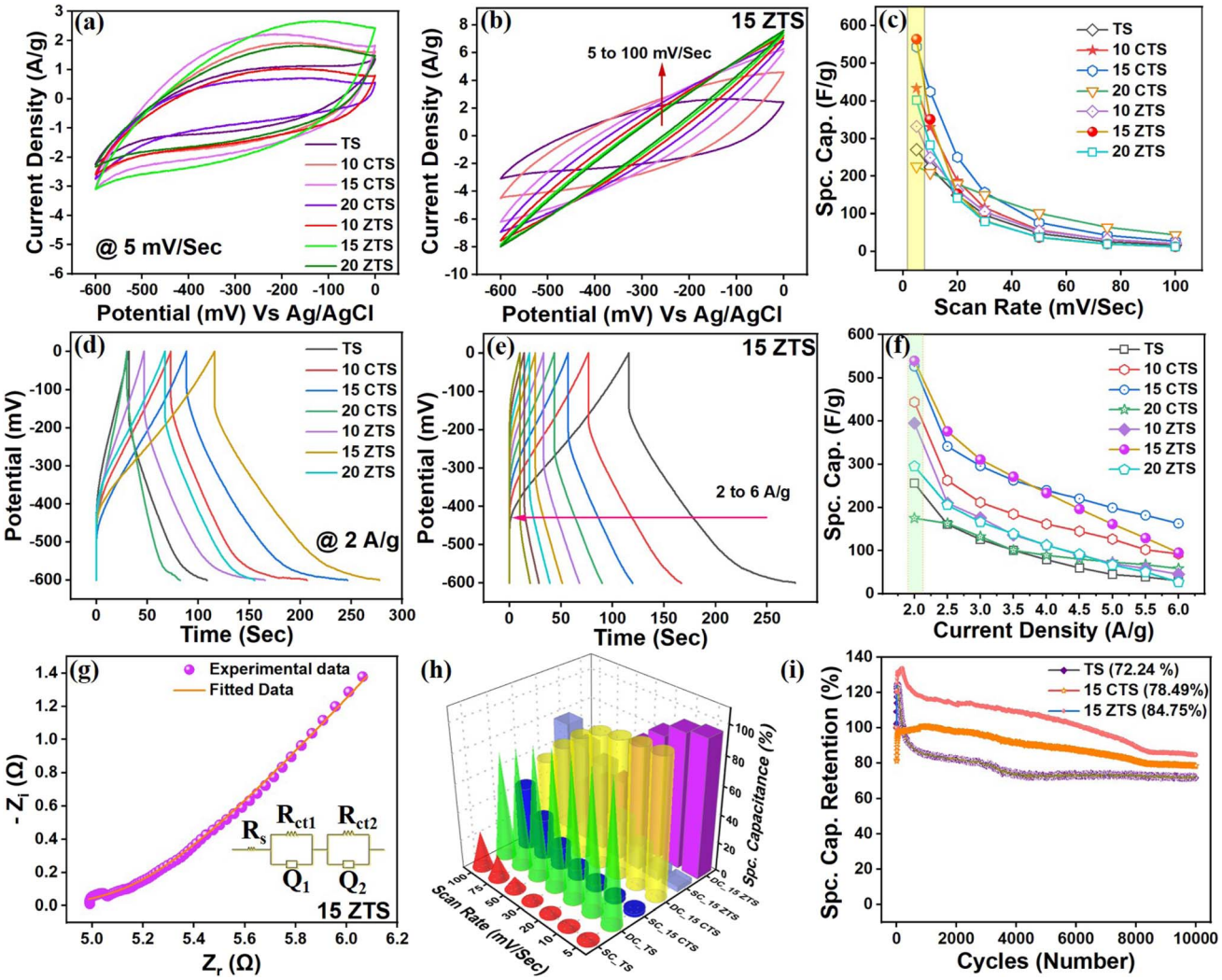

Fig. 3 (a) CV curves of individual compositions at 5 mV s^{-1}, (b) voltammograms of 15ZTS at various scan rates (5 to 100 mV s^{-1}), (c) retention performance of all compositions across scan rates, (d) GCD curve at a current density of 2 A g^{-1} for all compositions, (e) GCD curves of 15ZTS at various current densities (2 to 6 A g^{-1}), (f) retention capability of TS and 10, 15, and 20Z/CTS at various current densities, (g) EIS curves of 15ZTS, (h) comparative plot of calculated surface and diffusion-controlled capacitance (by Dunn's method) of TS and 15Z/CTS, and (i) specific capacitance retention of TS and 15Z/CTS after 10 000 CV cycles.

Fig. 3e displays the GCD curve of 15ZTS at current densities between 2 and 6 A g^{-1} at increments of 0.5 A g^{-1}. At 1 A g^{-1} current density, the working electrode displayed incomplete discharge, signifying sluggish and limited charge transfer at the electrode surface. At a current density of 2 A g^{-1}, the specific capacitance values of 15ZTS, 15CTS, and TS are calculated to be 539.96, 526.92, and 255 F g^{-1}, respectively. The GCD curves of TS, 10, 15, and 20 CTS along with 10 and 20 ZTS are presented in SI Fig. S5. A detailed representation of specific capacitance measurements for each electrode at various scan rates and current densities is presented in SI Table S1. Fig. 3f shows consistent capacitance behaviour at changing current densities. Lower current densities result in higher specific capacitance due to a more uniform charge–discharge process, allowing sufficient time for ion diffusion and optimal utilization of active sites. At elevated current densities, the IR drop (ohmic drop) increases because of higher resistance in electrolyte transport and charge transfer.

Electrochemical impedance spectroscopy (EIS) was used to investigate the kinetics of reactions at the electrode–electrolyte interface, covering a frequency range of 100 kHz to 0.01 Hz at an alternating current amplitude of 5 mV. Fig. 3g presents the impedance spectra of 15ZTS obtained in the aforesaid range. The equivalent circuit used to fit the impedance spectra is provided in the inset of Fig. 3g. All the impedance responses of each and every individual combination are provided in SI Fig. S6. The R_s in the equivalent circuit represents the electrolyte resistance offered by the electrolyte ions during the potential driven ion diffusion. R_{ct1} and R_{ct2} stand for the charge transfer resistance between the electrode material and electrolyte ion interaction at the electrode electrolyte interface. The circuit parameter Q represents the constant phase element (CPE) used to denote the non-idealistic behaviour of the electrode and electrolyte ion interaction. Q_1 and Q_2 reflect nonideal behaviour relative to an ideal capacitor framework. The CPE is given using eqn (1),

$$Q\,(\mathrm{CPE}) = [T_{\mathrm{CPE}}\,(j\omega)^n]^{-1} \quad (1)$$

where ω is the angular frequency, T_{CPE} is the constant phase coefficient, j is the imaginary number $(-1)^{1/2}$ and n is the exponent. The irregularities in charge storage mechanisms can be deduced from the exponent value, where the inductor, resistor, redox dominated capacitive element and ideal electrostatic capacitive element are represented by the values $n = -1$, 0, 0.5 and 1, respectively. The parametric values of each circuit element are tabulated in SI Table S2. The reduction in the R_s value in 10, 15, and 20C/ZTS as compared to those of TS shows efficient charge transfer at the composite interface. 15ZTS shows the least R_s value of 4.85 Ω showing the optimal efficiency for fast charge transfer. The Q_1-n exponent shows the behavioural pattern of the electrode in the higher frequency region. The values of Q_1-n for TS, 15CTS and 15ZTS are found to be 0.19, 0.17 and 0.51, respectively. The Q_1-n increment trend can also be confirmed in the 10, 15, and 20CTS and 10, 15, and 20ZTS nanocomposites confirming the effective surface reduction and oxidation reaction between the active electrode material and H_2SO_4 electrolyte ions. The sheet like nanoflower of ZCO integrated with the layered sulphonated sheets of TS contributes effectively due to its higher surface availability. The reduction in the value of R_{ct1} in 10, 15, and 20ZTS corresponding to the Q_1-CPE indicated the superior charge transfer efficiency as compared to that of TS and 10, 15, and 20CTS. Similarly, in the lower frequency region the charge interaction is found to be dominated by surface dominated electrostatic charge interaction. The Q_2-n exponent for 10, 15, and 20CTS along with 10, 15, and 20ZTS is found to be 1, which confirms the surface dominated electrostatic charge interaction. The increase in the Q_2-n value from 0.745 to 1 in the case of composites confirms the synergetic enhancement due to integration of ZCO and CCO. A similar trend of reduction in the value of R_{ct2} can be observed in SI Table S2, indicating efficient charge transfer of 10, 15, and 20ZTS as compared to TS and 10, 15, and 20CTS.

The detailed electrochemical response of ZCO and CCO is provided in SI Fig. S7 and S8, respectively. The specific capacitance of ZCO and CCO are calculated to be 10.04 and 3.24 F g^{-1} at a 5 mV s^{-1} scan rate. R_s values corresponding to ZCO and CCO are found to be 3.68 and 5.6 Ω, suggesting efficient faster charge interaction in the case of ZCO. The exponent value n_1 corresponding to Q_1 is found to be 0.76 suggesting a hybrid (both electrostatic and redox dominated ion interaction) charge storage mechanism at higher frequency. The value of the exponent corresponding to Q_2 measured was obtained to be 0.45 which validates the dominance of redox mechanisms in ion interaction at lower frequencies. This indicates that the enhancement in specific capacitance is due to composite formation with TS. In ZTS and CTS, the active conductive network at the TS and ZCO/CCO interface acts as the synergetic root for electrolyte ion interaction at the perovskite sites. A similar frequency determined behaviour can be observed in CCO as the values of Q_1-n and Q_2-n are found to be 0.96 (electrostatic) and 0.49 (redox), respectively. The R_{ct1} values corresponding to ZCO and CCO are found to be 0.53 and 0.63 Ω, suggesting efficient surface redox reaction dominated charge transfer in the case of ZCO. Similarly, efficient surface electrostatic charge transfer can be confirmed by the lower value of R_{ct2} in ZCO as compared to CCO as shown in tables included in SI Fig. S7 and S8.

To differentiate between capacitive and diffusion-controlled charge storage mechanism contributions in the overall performance of supercapacitors Dunn's power method was used. The individual contribution can be quantified by using eqn (2)

$$i = k_1 v + k_2 v^{1/2} \quad (2)$$

where v is the scan rate, i is the current at a specific voltage, $k_1 v$ corresponds to electrostatic non-faradaic charge interaction, and $k_2 v^{1/2}$ denotes the diffusive redox contributions shaping the complete CV resultant profile. Fig. 3h highlights the distinct contributions and the improvement in diffusion-controlled charge interactions observed in 15ZTS and 15CTS. The combination of CCO and ZCO with the layered TS structure increases the electrolyte ion drift towards the active sulphonate ions,

facilitating greater interaction with the electrolyte and promoting diffusion-dominated charge storage through enhanced redox activity. At 5 mV s^{-1} the domination of diffusion-controlled behaviour can be observed by 98.39, 96.07 and 97.77% in the case of TS, 15ZTS and 15CTS, respectively.

The enhanced redox-active sulfonated surface aligns well with BET surface area results and the Q_1 value obtained from the EIS equivalent circuit. The individual bar diagrams of TS, 15CTS and 15ZTS showing the individual contribution are shown in Fig. S6a–c, respectively. The contribution of the surface controlled EDLC type charge interaction can be confirmed by the enhancement in the surface-controlled behaviour at 100 mV s^{-1}. A comparison table showing the individual contribution of surface and diffusion-controlled behaviour of TS, 15ZTS and 15CTS at various scan rates is provided in the SI (Table S3). The contribution of surface-controlled charge interaction is dominant in the case of 15ZTS as compared to 15CTS. This can be attributed to the nanosheets integrating into nanoflower morphology of ZCO as compared to CCO. This enhancement is consistent with the Q_2 exponent values obtained in EIS analysis showing the EDLC type ion interaction. The surface contribution enhancement is consistent with the surface area observed in BET and BJH analysis. Fig. 3i illustrates the capacitive retention of TS and 15Z/CTS over 10 000 cycles, validating its suitability for repeated operational cycles. Specific capacitance grows with cycling, driven by improved wettability and ion penetration, but decreases later due to saturation of ions at the electrode interface. After 10 000 CV cycles TS, 15CTS and 15ZTS retains 72.24, 78.49 and 84.75% of S_c obtained in the initial cycle, respectively. At limited doping (10%), perovskite crystals can struggle to build a continuous network, hence limiting charge transport. At 15%, the perovskite can reach a percolation threshold, facilitating efficient charge transport channels through the MXene conductive matrix. At 20 wt%, excessive spinel interrupts the MXene network and increases series resistance (R_s increases from 4.85 Ω at 10ZTS to 6.66 Ω at 20ZTS), lowering performance. A higher wt% composition of perovskite in MXenes provides its own active area as compared to MXene reducing the synergetic effect in charge storage. A comparison table showing the electrochemical performance of 15ZTS and 15CTS with similar work is provided in SI Table S4. With regard to allied studies, this study presents a cost-effective grafting of redox-active sulfonate sites onto MXene surfaces, coupled with nanoflower-like spinel perovskite integration, yielding synergistically enhanced electrochemical performance. The hydrothermally synthesized MnO_2_MXene composite showed the highest specific capacitance of 242 F g^{-1} at 1 A g^{-1} in 0.5 M K_2SO_4 electrolyte.[57] $MnCo_2O_4$ and $ZnCo_2O_4$ integrated with MXenes *via* a hydrothermal method showed high specific capacitance but showed poor cycling stability after 5000 cycles.[58,59] By the electrochemical deposition technique of $NiCo_2S_4$ the fabricated supercapacitor with MXene exhibited the highest specific capacitance of 167.28 F g^{-1} at 4 A g^{-1} current density in 0.5 M K_2SO_4 electrolyte.[60] The study introduces a facile grafting approach that eliminates synthesis-related stoichiometric constraints, ensuring retention of MXene's inherent electrochemical behaviour. 15ZTS and 15CTS showed specific

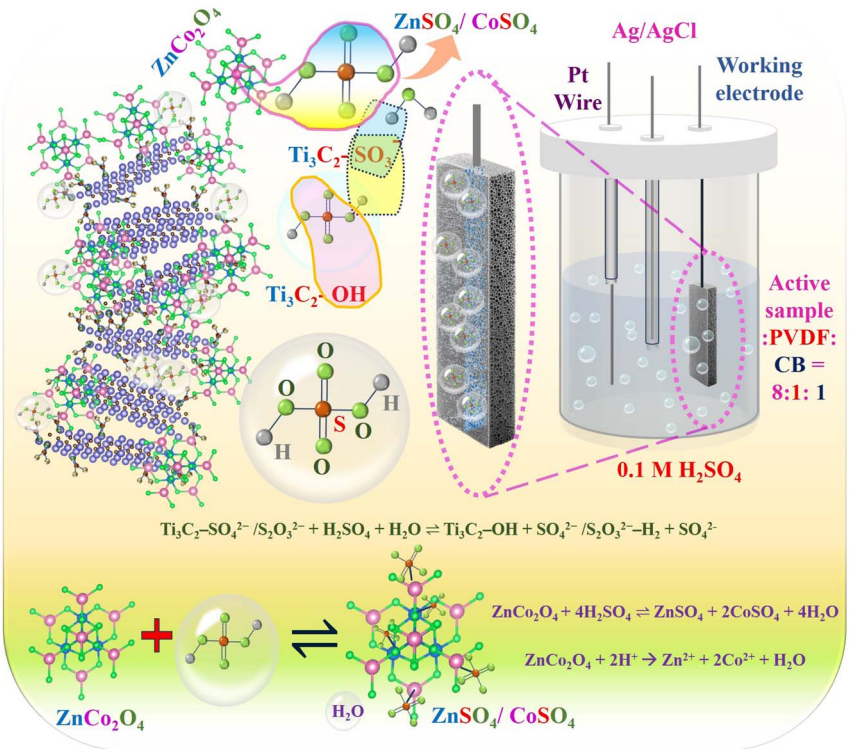

Fig. 4 Illustration of the redox-mediated interactions occurring within the $SO_4^{2-}/S_2O_3^{2-}$ ions present in TS integrated with $ZnCo_2O_4$ in H_2SO_4 aqueous electrolyte.

capacitances of 564.11 and 543.38 F g^{-1}, respectively, with excellent cycling stabilities (84.75% and 78.49% after 10 000 cycles) in a light electrolyte medium.

Fig. 4 illustrates the effective interaction of the H_2SO_4 electrolyte, facilitated by the increased presence of redox-active $SO_4^{2-}/S_2O_3^{2-}$ ions in TS and the incorporated ZCO. Eqn (3)–(6) present the active interaction reaction of ZTS comprehensively.

$$Ti_3C_2\text{–}SO_4^{2-}/S_2O_3^{2-} + H_2SO_4 + H_2O \rightarrow Ti_3C_2\text{–}OH + SO_4^{2-}/S_2O_3^{2-}\text{–}H_2 + SO_4^{2-} \quad (3)$$

$$Ti_3C_2\text{–}OH + SO_4^{2-} + H_2\text{–}SO_4^{2-}/S_2O_3^{2-} \rightarrow Ti_3C_2\text{–}SO_4^{2-}/S_2O_3^{2-} + H_2SO_4 \quad (4)$$

$$ZnCo_2O_4 + 4H_2SO_4 \rightleftharpoons ZnSO_4 + 2CoSO_4 + 4H_2O \quad (5)$$

$$ZnCo_2O_4 + 2H^+ \rightarrow Zn^{2+} + 2Co^{2+} + H_2O \quad (6)$$

Analogously, CCO contributes to the electrochemical process in a manner consistent with the reactions detailed in eqn (7) and (8):

$$CuCo_2O_4 + 4H_2SO_4 \rightleftharpoons CuSO_4 + 2CoSO_4 + 4H_2O \quad (7)$$

$$CuCo_2O_4 + 2H^+ \rightarrow Cu^{2+} + 2Co^{2+} + H_2O \quad (8)$$

Under cyclic driven potential, $SO_4^{2-}/S_2O_3^{2-}$ ions present in TS undergo reversible reactions with H^+ ions in H_2SO_4 electrolyte. Z and Co in ZCO, along with Cu, and Co in CCC, individually take part in the potential-induced electrochemical redox reaction. Eqn (6) and (8) represent the involvement of Co in the redox mechanism through the oxidation of Co^{3+} to Co^{2+}.

To demonstrate practical applicability, a symmetric (ZTS||ZTS) supercapacitor (ZTS_SS) was fabricated. The measurements of ZTS_SS devices were performed within the same operating potential window as done using the 3 electrode set up. Fig. 5a and b show the CV curves at scan rates from 5 to 100 mV s^{-1} and GCD curves at current densities from 2 to 5 A g^{-1}, respectively. Fig. 5c presents the electrochemical impedance spectra obtained in the range from 100 kHz to 0.01 Hz at an applied ac amplitude of 5 mV. The specific capacitance of ZTS_SS is found to be 119.12 F g^{-1} at a 5 mV s^{-1} scan rate and 129.13 F g^{-1} at 2 A g^{-1} current density. The retention of specific capacitance with respect to scan rate and current density is presented in Fig. 5d and e, respectively. The equivalent circuit parameters reveal a small electrolyte resistance $R_s = 5.19\ \Omega$ suggesting a uniform ion flow within the separator. The value corresponding to exponents of circuit element Q_1 was found to be 0.56 indicating redox dominated charge storage due to the surface functional sulphonate group of TS. The value of n_2 corresponding to Q_2 is found to be 1 indicating electrostatic charge interaction (due to the nanosheets of ZCO). A comparable indication of faster charge dynamics driven by redox dominated charge interaction at the electrode interface is reflected in the reduced R_{ct1} value of 6.05 Ω. The sluggish charge transfer in EDLC dominated charge interaction in the ZTS_SS device can be indicated by the R_{ct2} value of 141.2 Ω. After 5000 CV cycles the ZTS_SS device shows 65.6% retention of the initial specific capacitance value as presented in Fig. 5f. The initial increment in the specific capacitance with cycle count is due to the enhancement in wettability and ion penetration characteristics of the active current collector. This process improves its interaction with the ions present in the electrolyte. The decline in the specific capacitance value with the cycle number can be ascribed to the electrolyte ion saturation at the electrode interface. The calculations for the energy and power densities of the prototype device were performed using eqn (9) and (10), respectively.

$$E = \frac{1}{2} S_c \cdot (\Delta V)^2 \frac{1}{3.6}\ \text{Wh kg}^{-1} \quad (9)$$

$$P = \frac{E(3600)}{t}\ \text{W kg}^{-1} \quad (10)$$

where E denotes the energy density, P represents the power density, S_c signifies the specific capacitance, ΔV corresponds to the active potential window, and t refers to the discharge time.[61] The energy and power densities are calculated to be 6.45 Wh kg^{-1} and 598.48 W kg^{-1}, respectively, as shown in the Ragone plot (Fig. 5g). Fig. 5h depicts an open-side perspective of the SS device fabrication process, with comprehensive details outlined in the experimental methodology section. The operational feasibility of ZTS_SS was demonstrated by its ability to power arrays of six LEDs operating at different forward voltage levels. Fig. 5i shows the charge and discharge time for the array of LEDs. A series combination of two ZTS_SS was charged using a DC supply and discharged through the array of LEDs. For 20 s of charging, the device showed discharge times of 100, 84, 62, 35 and 35 seconds for red, yellow, green, blue and white LEDs, respectively. The charging and discharging behaviour of ZTS_SS using an array of LEDs is presented in a video link (**https://drive.google.com/file/d/1cIxDMXX4BIY6hBXYbnbItEs3hvm-3Ac4/view?usp=sharing**) provided in the SI.

Fig. 6a–d present side-view geometries of Ti_3C_2-based supercells with varying surface functional groups, offering a clear perspective on how structural modifications influence their electronic behaviour. In the pristine structure shown in Fig. 6a, for Ti_3C_2 (TM), a layered configuration is visible, exhibiting typical MXene behaviour with evenly distributed Ti and C atoms. This unfunctionalized phase serves as a baseline to understand the electronic changes after functional group introduction. Upon SO_3^{2-} functionalization as seen in Fig. 6b, the structure transforms into Ti_3C_2–SO_3^{2-} (TS). Here, the introduction of sulfonate groups increases the interlayer spacing slightly, promoting improved accessibility for electrolyte ions. The functional group also induces partial charge redistribution across the surface, potentially enhancing electrochemical redox activity due to newly exposed active sites. Further modifications in Fig. 6c and d show ZTS and CTS configurations, respectively. ZTS combines integration of the $ZnCo_2O_4$ crystal site attached at the Zn-site and sulfonate functionalities. This contributes to increased electron density near the Fermi level and modulates density of states (DOS). This tailoring is beneficial for improving pseudocapacitive

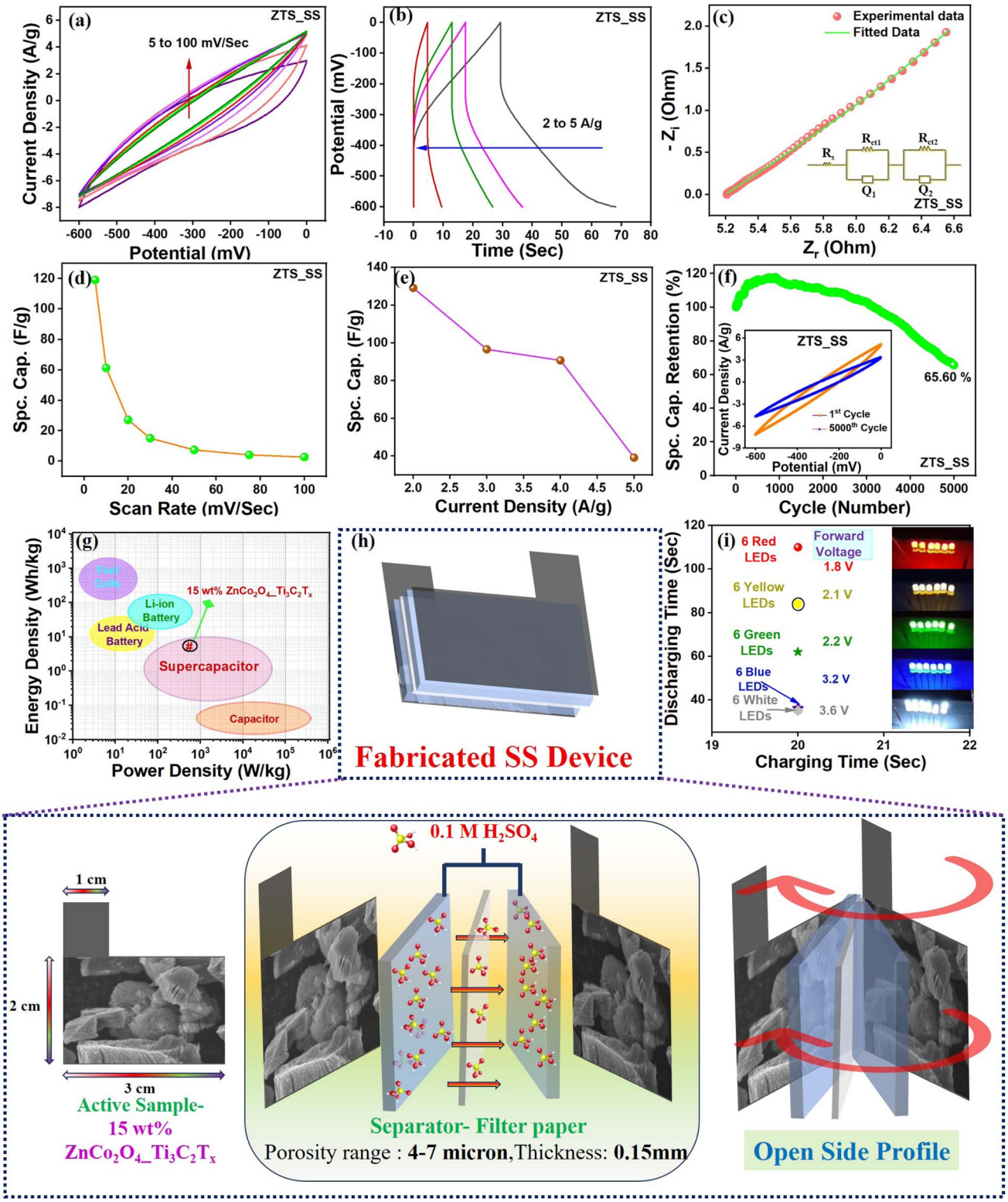

Fig. 5 (a) CV curve, (b) GCD curve, (c) EIS spectra of ZTS_SS (inset-shows the fitted equivalent circuit), retention of specific capacitance with respect to (d) scan rate and (e) current density, (f) cyclic testing shows 65.6% performance retention over 5000 cycles, (g) Ragone plot, (h) illustration of fabrication of the ZTS_SS device and (i) the charge and discharge of an array of 6 LEDs of various forward voltages.

responses. Similarly, CTS includes integration of Cu-sites of the $CuCo_2O_4$ crystal along with SO_3^{2-}, altering the surface chemistry significantly. These dual-functionalized models show more pronounced orbital hybridization between Ti d-orbitals and O/S atoms, which may enhance charge transfer kinetics. The supercell theoretical models favour enhanced charge storage,

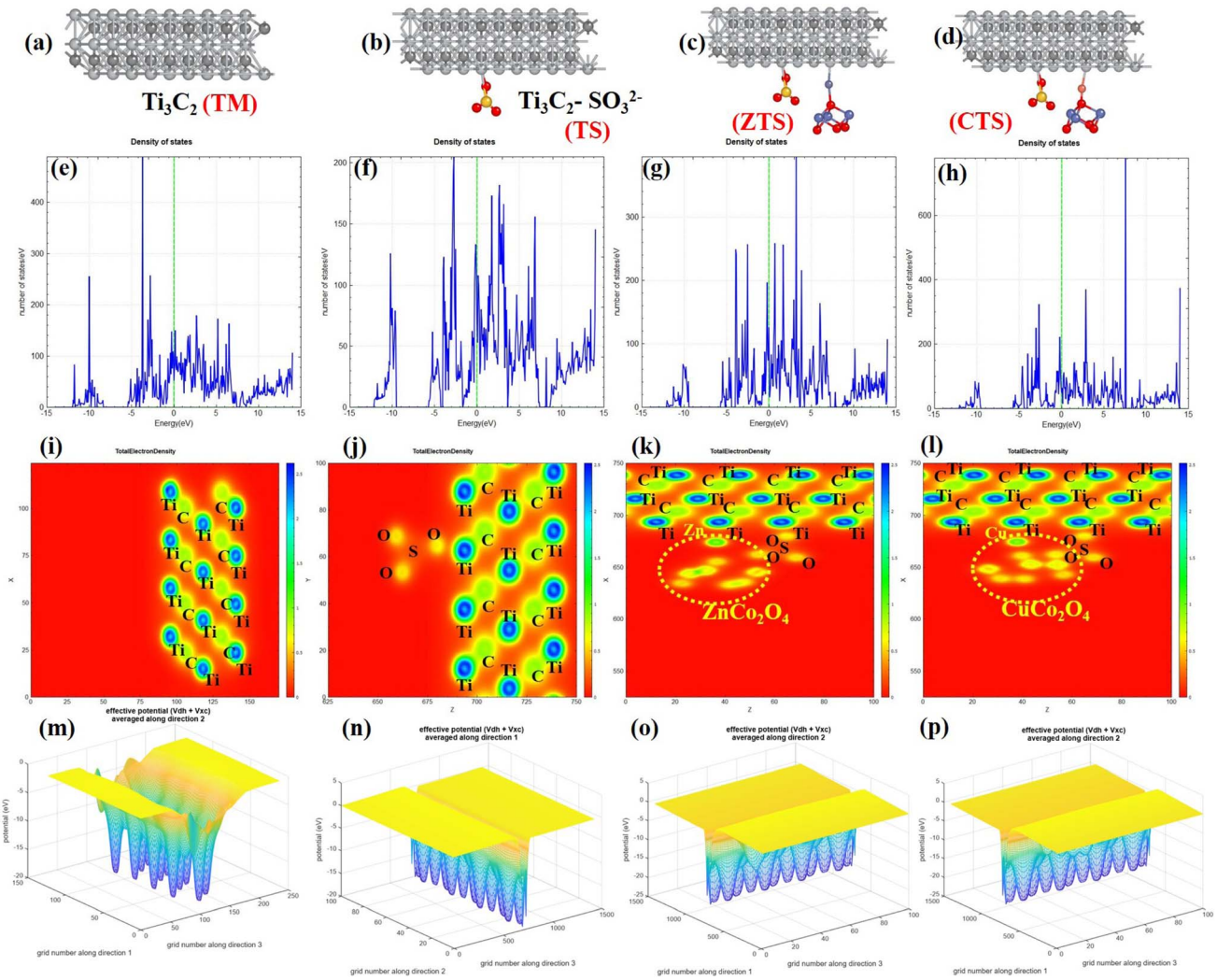

Fig. 6 Theoretical investigation of $Ti_3C_2T_x$-based configurations: (a–d) side-view atomic models of pristine Ti_3C_2 (TM), sulfonated Ti_3C_2 (TS), $ZnCo_2O_4$-anchored Ti_3C_2 (ZTS), and $CuCo_2O_4$-anchored Ti_3C_2 (CTS); (e–h) corresponding total density of states (DOS) profiles; (i–l) charge density maps highlighting electron delocalisation and interfacial bonding; (m–p) effective potential distributions visualising electrostatic field modulation.

faster ion diffusion, and stability, making them ideal candidates for designing high-performance $Ti_3C_2T_x$ based hybrid electrode systems with 3D ZCO/CCO frameworks for advanced supercapacitor applications.

The density of states (DOS) plots presented in Fig. 6e–h offer a deep theoretical understanding of how surface functionalisation affects the electronic structure of the $Ti_3C_2T_x$ supercell. In the unmodified Ti_3C_2 (TM) model (Fig. 6e), the DOS curve displays a significant peak close to the Fermi level. This prominent feature points towards the material's ability to facilitate smooth electron movement, which is quite essential for efficient charge transport in energy storage devices like supercapacitors. Upon introducing sulfonate (SO_3^{2-}) groups to create the TS configuration (Fig. 6f), one can observe evident changes in the DOS pattern. There is an increase in the electronic states near the Fermi level, along with the appearance of new features in the conduction band. These alterations are primarily due to the bond interactions involving oxygen and sulphur atoms, which promote better orbital overlap and electron delocalisation. This enhanced interaction may help in storing more charge by enabling redox-related energy storage. In the ZTS variant (Fig. 6g), which includes both $ZnCo_2O_4$ and SO_3^{2-} functionalities, the DOS becomes wider and more complex with multiple peaks. This shows that the involvement of Zn atoms has strengthened the internal electronic interactions within the system. As a result, quicker ion diffusion and dual-mode charge storage through both EDLC and pseudocapacitive effects become possible which can be evidenced from the Q_1 exponent value ($n_1 = 0.76$) obtained in EIS for ZCO. The CTS structure (Fig. 6h), with $CuCo_2O_4$ and SO_3^{2-} decoration, displays an even denser distribution of states near the Fermi level. This structure encourages faster electron mobility and enhanced energy transfer, which are favourable for high-performance hybrid supercapacitor systems. Thus, surface functionalisation emerges as a key strategy for tuning the electronic framework of $Ti_3C_2T_x$, ultimately leading to improved energy storage

capabilities when integrated with ZCO and CCO nanostructures. Among all configurations, the ZTS structure exhibits the most diversified and intensified DOS profile, especially near the Fermi level. This abundance of accessible electronic states ensures improved redox activity and faster electron transport, thereby enhancing both electrochemical double-layer capacitance and pseudocapacitive responses essential for high-efficiency supercapacitor performance.

The total energy density mappings shown in Fig. 6i–l offer valuable theoretical insight into the charge redistribution and interaction potential within various $Ti_3C_2T_x$-based configurations. In the unmodified Ti_3C_2 (TM) structure (Fig. 6i), the electron cloud is relatively confined around the Ti atoms, with a clear, symmetrical distribution pattern. The low distortion and compact energy density hint at a structurally stable system, yet with limited active interaction with external functional species. Upon surface functionalisation with sulfonate groups (TS, Fig. 6j), the energy distribution becomes more diffused. The presence of oxygen and sulphur atoms induces notable charge polarization, resulting in stronger localised interactions. These zones indicate enhanced electron affinity and bonding strength, which can contribute to improved ionic adsorption and redox reactivity, factors critical for efficient charge storage. A complex energy landscape is observed in the ZTS model (Fig. 6k), where $ZnCo_2O_4$ is coupled with the sulfonated MXene surface. Here, distinct zones of energy intensification are marked by interactions between Ti, Zn, O, and S atoms. These enriched zones of electron delocalisation suggest synergistic bonding, promoting faster ion transport and greater electrochemical activity, suitable for hybrid supercapacitor systems. Similarly, the CTS configuration (Fig. 6l), involving $CuCo_2O_4$ integration, reveals dense energy contours across the interface. The copper-rich regions foster strong electron overlap with the sulfonate-functionalised $Ti_3C_2T_x$ layer, facilitating efficient charge relay mechanisms. This enhanced electronic coupling could lead to better cycling stability and energy delivery under high current loads. The total electron density mapping of ZTS reveals rich zones of charge delocalisation and orbital overlap between Ti, Zn, S, and O atoms. This synergistic redistribution of charge, consistent with the elevated DOS, facilitates robust interfacial bonding and accelerates ion diffusion, making ZTS a highly responsive and stable platform for energy storage.

The effective potential landscapes depicted in Fig. 6m–p offer an internal electrostatic environment across the $Ti_3C_2T_x$ systems under various functionalisation and composite frameworks. In the pristine Ti_3C_2 (TM) configuration (Fig. 6m), a sharp gradient in potential is clearly visible near the atomic layers. The deeper valleys suggest a strongly confined electron distribution around Ti atoms, indicative of a robust internal field but with limited tunability in terms of interfacial interactions. Upon sulfonate modification (TS, Fig. 6n), the potential profile becomes more homogenised along the interlayer spacing. The smooth potential troughs, though not as steep as in TM, reflect a redistributed electrostatic field due to the nucleophilic nature of sulphur and oxygen atoms. The modification subtly reduces potential barriers, favouring ion accommodation and interface stabilisation, which are critical in electrochemical double-layer formation. A more refined and shallower potential well appears in the ZTS configuration (Fig. 6o), which includes ZCO integration. The evenly modulated surface energy indicates efficient charge screening and smoother electron migration pathways. Such a potential field fosters rapid charge–discharge cycles, allowing better electrochemical kinetics crucial for hybrid capacitors. Similarly, the CTS model (Fig. 6p), embedded with CCO, showcases a remarkably uniform and elevated potential surface. The Cu site-mediated hybrid interface seems to enhance the electrostatic stability while preserving surface reactivity. This can significantly influence the electrode–electrolyte interface dynamics, supporting sustained ionic flux and high capacitance retention during cycling. The effective potential findings substantiate the improved energy storage behaviour in $Ti_3C_2T_x$ systems interfaced with ZCO and CCO, paving the way for efficient and robust supercapacitor applications. The ZTS model demonstrates a refined and evenly distributed potential landscape with shallower wells and minimal barriers. This modulated electrostatic field enhances ionic mobility and fosters rapid charge–discharge dynamics. The harmonised potential profile not only stabilises the electrode–electrolyte interface but also supports prolonged cycling with minimal capacitance fade.

The DOS of sulphonated MXene (TS) shows enhanced electronic states near the Fermi level (E_F) compared to pristine Ti_3C_2 (TM), consistent with the reduced charge transfer resistance (R_{ct}) observed in EIS. Incorporating ZCO or CCO nanoparticles onto the sulphonated MXene surface induces a prominent restructuring of the electronic DOS. The emergence of additional transition-metal d-states within ± 1 eV of the E_F reflects the strong electronic coupling between the spinel oxide and the MXene substrate. These introduced states act as accessible electronic channels, effectively bridging the energy gap between filled and unfilled states, which is critical for rapid redox transitions during charge–discharge processes. The observed band edge broadening extends the continuum of available energy levels, facilitating a multi-channel charge-transfer mechanism that allows simultaneous electron flow through different conduction pathways. This is confirmed by the reduction in the R_s (series resistance offered by the electrolyte ions) value from 6.02 to 4.8 and 5.2 Ω in the case of TS, 15ZTS and 15CTS, respectively. This broadened DOS profile is directly correlated with the experimentally observed improvements in electrochemical performance. The increased density of accessible states near E_F enhances intrinsic conductivity, while the synergistic redox contributions from Co^{2+}/Co^{3+} couples in the spinel phase complement the capacitive response of the MXene. Cyclic voltammetry shows more pronounced redox dominated charge storage (by Dunn's method analysis) and larger integrated areas, while galvanostatic charge–discharge curves reveal reduced IR drop and higher specific capacitances. The combination of sulphonate functionalisation and spinel oxide anchoring thus provides an optimised interface for efficient ion diffusion and electron transport, underpinning the superior rate capability and exceptional cycling stability observed in experiments.

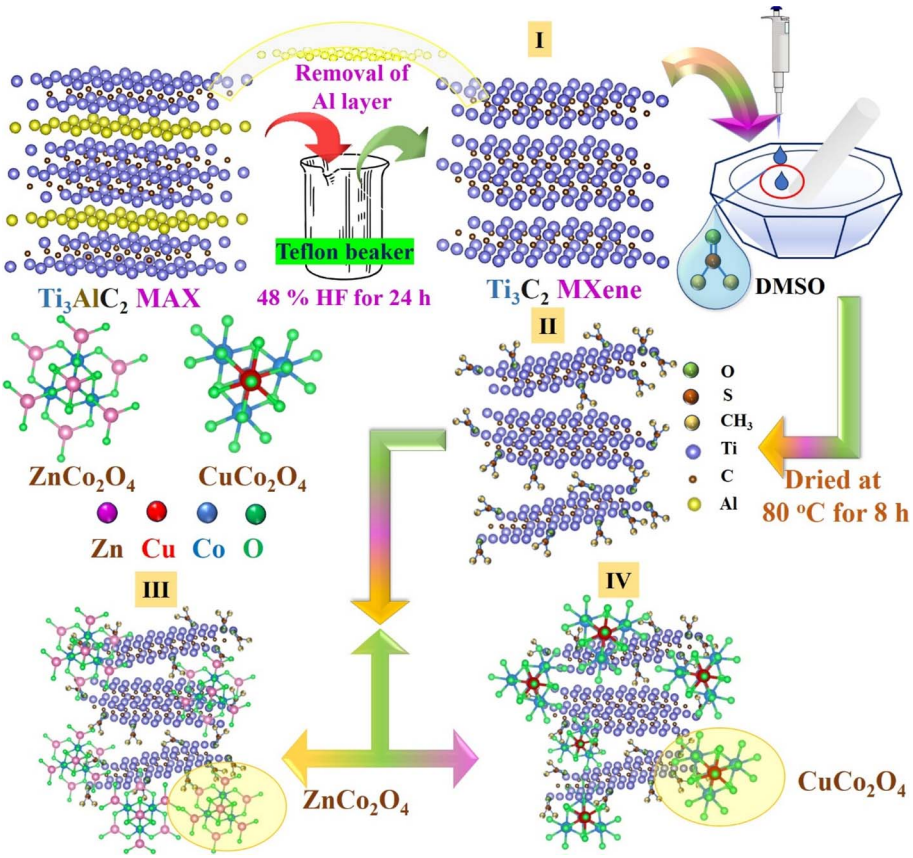

Scheme 1 Schematic illustrating $Ti_3C_2T_x$ synthesis from Ti_3AlC_2 *via* HF etching (step I), sulfonation with DMSO (step II), and incorporation of $ZnCo_2O_4$ (step III) and $CuCo_2O_4$ (step IV) by grinding in DMSO solvent and drying at 80 °C for 8 h.

3. Conclusion

In summary, a cost-effective grinding process successfully functionalized the MXene surface with sulphonate ions using DMSO, enabling redox active interaction in an aqueous electrolytic medium. Additional improvement in electrochemical energy storage of TS was achieved through perovskite (ZCO and CCO) nanoflower incorporation (at 10, 15 and 20 wt%). The increase in ion-interactive surface area was verified by BET analysis. Specific capacitance increases due to fast redox reactions in 15ZTS and 15CTS were confirmed by EIS and Dunn's method analysis. The practicability of 15 wt% ZCO integrated sulphonated MXene (15ZTS) was tested by using a glowing array of LEDs (with various forward voltages) and it showed 65.6% specific capacitance after 5000 cycles. The energy and power densities are calculated to be 6.45 Wh kg^{-1} and 598.48 W kg^{-1}, respectively. The theoretical calculations confirm DOS, energy density profiles, and effective potential and clearly show how surface functionalisation of $-SO_3$ and composite (ZTS and CTS) integration actively reshape the electron environment, enabling superior charge storage properties ideal for next-generation supercapacitor devices. This dual-pronged approach not only strengthens the scientific depth of the work but also guides intelligent material design for next-generation energy storage devices.

4. Experimental methods

4.1. Materials used

The Ti_3AlC_2 MAX phase (99.99% purity with an average particle size of 40–60 mm, NANOSHEL, India) and hydrofluoric acid (HF, 48%, FINAR, INDIA) were used for MXene synthesis. Zinc nitrate hexahydrate, cobalt nitrate hexahydrate, and cupric nitrate trihydrate were procured from FINAR, India, each with 99.99% purity. 1 mm graphite sheets were obtained from Thermo Scientific chemicals. The tissue paper (10 GMS, 3 Ply) used during device fabrication was obtained from Origami Cellulo PVT Ltd, India. Polyvinyl difluride (PVDF) and conductive carbon black were obtained from Sigma Aldrich. Dimethylsulphoxide (DMSO, AR, 99.99%) was obtained from SRL India.

4.2. MXene synthesis and its functionalisation with sulphonate groups

$Ti_3C_2T_x$ MXene (TM) synthesis was achieved through the hydrofluoric acid (HF) etching approach as described in step-I of Scheme 1. The selection of HF for MAX phase processing is based on its ability to efficiently and selectively etch A-site elements (A, often Al, Si, or Ga), predominantly aluminium (Al), as part of the structure. Hydrofluoric acid (HF) was selected for its ability to readily form AlF_3, while minimally disturbing the transition metal (M) and carbon (X) layers.[62] HF effectively

extracts Al from the Ti_3AlC_2 MAX phase, giving rise to a structured MXene layer. A 100 ml Teflon beaker was filled with 30 ml of 48% concentrated HF, (Alfa Aesar). During continuous stirring at 150 rpm, 2 g of Ti_3AlC_2 powder was slowly introduced to mitigate heat production in the initial phase of the reaction and to control the rapid gas evolution.

Introducing the MAX phase at a controlled pace ensures improved structural integrity in the resulting MXene layers and facilitates homogeneous etching. For 24 hours, the MAX phase was treated with HF while stirring at 400 rpm at room temperature (35 °C). Subsequently, the mixture was washed multiple times with DI water (centrifuged at 5000 rpm for 15 minutes) until the supernatant reached a pH level of 6. Following the washing process, the mixture was filtered with Whatman filter paper (diameter: 15 cm; pore size: 11 mm), and the filtered material was dried at 80 °C for 8 hours to produce multilayered $Ti_3C_2T_x$ MXene. The process involved the selective removal of Al from Ti_3AlC_2 using HF, resulting in the formation of $Ti_3C_2T_x$ MXene as shown in the equations below.

$$Ti_3AlC_2 + 3HF \rightarrow AlF_3 + 3/2H_2 + Ti_3C_2 \quad (11)$$

$$Ti_3C_2 + 2H_2O \rightarrow Ti_3C_2(OH)_2 + H_2 \quad (12)$$

$$Ti_3C_2 + 2HF \rightarrow Ti_3C_2F_2 + H_2 \quad (13)$$

The etching reaction of Al through HF, depicted in eqn (11), generates hydrophilic AlF_3, which can be effectively eliminated during washing. Eqn (12) depicts the production of hydrogen gas, which occurs through the oxidation of Ti and the simultaneous reduction of H. The presence of unreacted HF can result in fluoride terminations forming on the MXene surface, as shown in eqn (13). Functionalisation of sulphonate groups at the MXene surface sites was done using dimethyl sulfoxide (DMSO) solvent. In this process, 50 mg of synthesized MXene was taken in an agate mortar and 500 μl of DMSO was added and ground for 20 min. The formation of sulphonate ions at the MXene surface was achieved by drying the resultant slurry at 80 °C for 8 h. As illustrated in step-II of the synthesis in Scheme 1, the interaction between DMSO and the hydroxyl group on MXene produces sulphonate ions that are attached to the surface. The surface sulphonation of the MXene sheet is represented in eqn (14).

$$Ti_3C_2\text{–}OH + 2C_2H_6SO\ (DMSO) \rightarrow Ti_3C_2\text{–}SO_4^{2-}/S_2O_3^{2-} + 4CH_3\uparrow \quad (14)$$

The termination of sulphonate ions at the MXene surface facilitates its active participation in the redox reaction in an H_2SO_4 electrolyte during the applied potential sweep. DMSO intercalation improves the electronic properties of MXenes by facilitating layer exfoliation, modifying surface functional groups, and enhancing electrical conductivity.

4.3. $ZnCo_2O_4$ synthesis

20 mM of cobalt nitrate hextahydrate, 10 mM zinc nitrate hexahydrate, and 150 mM urea were dissolved in 65 ml of DI water. The solution was then transferred to a Teflon lined autoclave and treated at 120 °C for 12 h. Then the hydrothermally treated solution was filtered and cleaned with DI water. The filtered sample was then dried overnight at 60 °C. The dried sample was then calcined at 350 °C for 2 h at a ramp rate of 5 °C min^{-1}. The obtained powder was ground and collected.

4.4. $CuCo_2O_4$ synthesis

20 mM of cobalt nitrate hextahydrate, 10 mM cupric nitrate trihydrate, and 150 mM urea were dissolved in 65 ml of DI water. After transferring the solution into a Teflon-lined autoclave, it was heated hydrothermally at 120 °C for 12 h. Subsequently, the hydrothermally processed solution underwent filtration and was rinsed using deionized water. The filtered sample was then dried overnight at 60 °C. The dried sample was then calcined at 650 °C for 2 h at a ramp rate of 5 °C min^{-1}. The powder, once obtained, was ground and carefully collected. A comprehensive hydrothermal synthesis schematic for $ZnCo_2O_4$ and $CuCo_2O_4$, highlighting calcination temperature changes, is displayed in SI Scheme S1.

4.5. Synthesis of the Zn/$CuCo_2O_4$ composite with sulphonated MXene

To investigate the enhancement in electrochemical interaction of sulphonate functional group modified $Ti_3C_2T_x$ MXene (TS), a lower wt% of ZCO/CCO was tested, minimizing any additional physiochemical impacts on MXenes by ZCO/CCO. At higher wt%, excessive nanomaterial loading can lead to agglomeration, reducing the available active surface area for reactions. Maintaining an optimized concentration of ZCO/CCO facilitates homogeneous dispersion, increasing the active surface area of TS accessible to the electrolyte. An overabundance of ZCO/CCO at the TS electrode interface could create diffusion barriers, hindering ionic mobility and reducing charge transfer efficiency in electrochemical energy storage systems. As discussed in the sulphonation of MXene sheets, the same slurry of MXene and DMSO was prepared. To prepare the individual compositions of $ZnCo_2O_4$ (ZCO) and $CuCo_2O_4$ (CCO) with sulphonated MXene, 10, 15 and 20 wt% of the synthesized materials are added to the above slurry and ground for 20 minutes. The mixture was dried at a temperature of 80 °C for 8 h as indicated in step III and IV of Scheme 1, and the resulting powder was taken for further analysis. The three compositions with 10, 15 and 20 wt% of ZCO in TS were named 10ZTS, 15ZTS and 20ZTS, respectively. Similarly, compositions with 10, 15 and 20 wt% of CCO in TS were named 10CTS, 15CTS and 20CTS, respectively. For electrode fabrication, the slurry solution of ZCO/CCO with TS is coated on nickel foam with a PVDF binder followed by drying.

4.6. Electrode preparation

The electrochemical analysis was performed at room temperature with a three-electrode setup, where a saturated Ag/AgCl electrode served as the reference and a Pt wire functioned as the counter electrode. The Ni foam (1×3 cm^2) designated as the working electrode was sonicated in 3 M HCl, deionized water, and absolute ethanol for 30 minutes per step to remove surface

impurities, and then dried at 80 °C for 12 hours. The active material slurry (ZCO, CCO, MXene, and ZCO/CCO-MXene in DMSO), combined with 10% activated carbon black and 10% PVDF binder were mixed to form a homogeneous mixture. The working electrode was prepared by drop-casting 8 mg of an activated material slurry onto a 1 × 1 cm^2 cleaned Ni foam substrate, which was then dried at 80 °C for 8 hours. 0.1 M H_2SO_4 aqueous solution was utilized as the electrolyte for all the electrodes. Specific capacitance of each electrode from CV and GCD curves were computed using eqn (15) and (16), respectively.

$$S_c = \frac{\int i \cdot dV}{m \cdot v \cdot \Delta V} \quad (15)$$

$$S_c = \frac{i \cdot \Delta t}{m \cdot \Delta V} \quad (16)$$

where S_c, i, ΔV, m and v stand for the specific capacitance, current, potential window, active mass loading on the electrode and scan rate, respectively. The numerator in eqn (5), $\int i \cdot dV$ represents the area under the CV curve (current to voltage response). The term Δt in eqn (6) represents the discharge time corresponding to the specific GCD curve at the given current density.

4.7. Two electrode device fabrication

A symmetric supercapacitor (SS) was fabricated to understand the precise material charge storage analysis ensuring a uniform electrochemical environment. A slurry was prepared with the active material (15ZTS), PVDF binder, and carbon black combined in the tested ratio of 8 : 1 : 1 with few drops of DMSO. This slurry was coated on two graphite sheets (2 × 3 cm^2) followed by drying at 80 °C for 8 h. The device was fabricated using tissue paper as a separator, which was fully wetted with a few drops of 0.1 M H_2SO_4. To ensure proper wettability and electrolyte ion accessibility at the electrode sides the fabricated device was pressed slightly and sealed with scotch tape. To test the ZTS_SS supercapacitor charge–discharge performance, an RC circuit was used.

4.8. Characterisation techniques

A Panalytical X-pert diffractometer with Cu Kα radiation (λ = 0.15406 nm) was employed to obtain XRD patterns. Functional group identification and modification were conducted through FTIR spectroscopy on an Alpha-II, Bruker, with crack-free KBr-active sample pellets. The X-Ray Photoelectron Spectroscopy (XPS) method was implemented using an ESCA+ Omicron Nanotechnology instrument. The Brunauer–Emmett–Teller (BET) and Barrett–Joyner–Halenda (BJH) methods, implemented through Quantachrome Instruments (version 5.23), were employed to analyze the surface area and pore size distribution. Morphological and elemental analysis was carried out with the help of FESEM (JEOL JSM IT-800). Electrochemical performance evaluations of the materials were conducted using an Origalys 500, Origa master, in a three-electrode configuration. A direct current (DC) power supply unit (PSD7303B, Scientific, India) was utilized to charge the fabricated symmetric supercapacitor device.

4.9. Theoretical calculations

The Nano Decal software has been utilised for density of states (DOS), total energy density and effective potential measurements of the Ti_3C_2 superlattice, sulphonated group attached to the Ti_3C_2 superlattice (TS-superlattice), and nanocomposite of ZCO and CCO with the TS-superlattice. The integration of Zn and Cu from ZCO and CCO, respectively into Ti positions of the TS superlattice has been examined. A plane-wave expansion was performed with a charge density cutoff of 225 Ry, while atomic structure relaxation used a 9 × 9 × 1 k-point mesh and a residual force convergence of 10^{-4} Ry $Å^{-1}$. The GGA-PBE96 approach by Perdew–Burke–Ernzerhof was adopted in Nano-Decal for DOS extraction.

Author contributions

Jitesh Pani: conceptualization, investigation, writing – original draft, validation, formal analysis. Hitesh Borkar: supervision, writing – review & editing, visualization.

Conflicts of interest

There are no conflicts to declare.

Data availability

Data will be made available upon reasonable request.

Supplementary information is available. See DOI: **https://doi.org/10.1039/d5ta05685c**.

Acknowledgements

JP acknowledges the Department of Science and Technology, Government of India for providing research grants under the INSPIRE fellowship (IF200298). HB acknowledges the financial support from the Department of Science and Technology, New Delhi ((ANRF) SERB-DST, file no EEQ/2022/001055). JP and HB would like to thank IMPULSE Technology for providing the trial version of NanoDecal software. JP and HB would like to thank the Director, NIT Warangal for his constant encouragement.

References

1 S. A. Hussain, F. Razi, K. Hewage and R. Sadiq, *Energy*, 2023, **275**, 127487.
2 M. Talaat, M. A. Farahat and M. H. Elkholy, *Energy*, 2019, **170**, 668–682.
3 A. G. Olabi, Q. Abbas, A. Al Makky and M. A. Abdelkareem, *Energy*, 2022, **248**, 123617.
4 M. Libber, N. Gariya and M. Kumar, *J. Solid State Electrochem.*, 2024, **29**, 513–527.
5 J. Zhao and A. F. Burke, *J. Energy Chem.*, 2021, **59**, 276–291.
6 D. P. Dubal, O. Ayyad, V. Ruiz and P. Gómez-Romero, *Chem. Soc. Rev.*, 2015, **44**, 1777–1790.

7 C. Zhong, Y. Deng, W. Hu, J. Qiao, L. Zhang and J. Zhang, *Chem. Soc. Rev.*, 2015, **44**, 7484–7539.
8 R. Ramachandran, Y. Wang, S. Chandrasekaran and M. Li, *Appl. Mater. Today*, 2022, **29**, 101578.
9 Y. Liu, C. Wang, H. Sun, L. Duan, Z. Yang, X. Wang and J. Liu, *J. Colloid Interface Sci.*, 2025, **682**, 1051–1061.
10 S. D. Jituri, S. M. Nikam, T. S. Bane, A. I. Inamdar and S. H. Mujawar, *Electrochim. Acta*, 2025, **513**, 145544.
11 P. Yadav, R. Yadav, J. Pani, R. M. Singh, D. Singh, K. Kumari, H. Borkar and J. Gangwar, *Dalton Trans.*, 2025, 3277–3286.
12 J. Pani, D. Maru, P. Chaudhary, J. Gangwar, K. U. Kumar, B. C. Yadav and H. Borkar, *Energy Technol.*, 2023, 1–11.
13 A. Ali, S. Ahmed, W. Jiang, G. Park and S. J. Oh, *Curr. Opin. Electrochem.*, 2025, **50**, 101640.
14 K. K. Swain, S. K. Pradhan and D. J. Late, *ChemistrySelect*, 2025, **10**, 1–25.
15 S. De, S. Acharya, S. Sahoo, A. K. Das and G. C. Nayak, *2D Materials for Solar Cell Applications*, 2021.
16 N. H. Solangi, N. M. Mubarak, R. R. Karri, S. A. Mazari and J. R. Koduru, *Int. J. Hydrogen Energy*, 2024, **73**, 905–931.
17 S. Ma, P. Xue, Y. Tang, R. Bi, X. Xu, L. Wang and Q. Li, *Responsive Mater.*, 2024, **2**, 1–30.
18 D. H. Ho, Y. Y. Choi, S. B. Jo, J. M. Myoung and J. H. Cho, *Adv. Mater.*, 2021, DOI: **10.1002/adma.202005846**.
19 S. Ghorbanzadeh and W. Zhang, *Nano Energy*, 2024, **125**, 109558.
20 X. Li, Z. Huang, C. E. Shuck, G. Liang, Y. Gogotsi and C. Zhi, *Nat. Rev. Chem.*, 2022, **6**, 389–404.
21 B. Anasori, M. R. Lukatskaya and Y. Gogotsi, *Nat. Rev. Mater.*, 2017, DOI: **10.1038/natrevmats.2016.98**.
22 Y. Zhou, J. Yang, N. Zhou, H. Hao, X. Jiang, F. Lei, K. Shi, Y. Zhao, G. Zhou, T. Liu and S. Xing, *Chem. Eng. J.*, 2023, **471**, 144647.
23 R. Ibragimova, P. Erhart, P. Rinke and H.-P. Komsa, *J. Phys. Chem. Lett.*, 2021, DOI: **10.1021/acs.jpclett.0c03710**.
24 Y. Lei, Y. Cui, Q. Huang, J. Dou, D. Gan, F. Deng, M. Liu, X. Li, X. Zhang and Y. Wei, *Ceram. Int.*, 2019, **45**, 17653–17661.
25 K. Wieszczycka, K. Staszak, M. J. Woźniak-Budych, J. Litowczenko, B. M. Maciejewska and S. Jurga, *Coord. Chem. Rev.*, 2021, DOI: **10.1016/j.ccr.2021.213846**.
26 K. M. Nell, S. A. Fontenot, T. G. Carter, M. G. Warner, C. L. Warner, R. S. Addleman and D. W. Johnson, *Environ. Sci.: Nano*, 2016, **3**, 138–145.
27 K. Montazeri, H. Badr, K. Ngo, K. Sudhakar, T. Elmelegy, J. Uzarski, V. Natu and M. W. Barsoum, *J. Phys. Chem. C*, 2023, **127**, 10391–10397.
28 S. Nahirniak, A. Ray and B. Saruhan, *Batteries*, 2023, DOI: **10.3390/batteries9020126**.
29 R. R. Arulanantham, A. D. Savariraj and V. Ragupathi, *J. Alloys Compd.*, 2025, **1022**, 179761.
30 A. K. Tomar, A. Joshi, G. Singh and R. K. Sharma, *Coord. Chem. Rev.*, 2024, DOI: **10.1016/J.CCR.2020.213680**.
31 L. Chen, J. Ding and X. Zhu, *RSC Appl. Interfaces*, 2025, **2**, 320–351.
32 Y. Cao, J. Liang, X. Li, L. Yue, Q. Liu, S. Lu, A. M. Asiri, J. Hu, Y. Luo and X. Sun, *Chem. Commun.*, 2021, **57**, 2343–2355.
33 M. Neelakandan, P. Dhandapani, S. Ramasamy, R. Duraisamy, S. J. Lee and S. Angaiah, *RSC Adv.*, 2025, **15**, 16766–16791.
34 Y. Zhang, Q. Zhong, Y. Bu, D. Meng, H. Gu, Q. Lu, Y. Zhao and G. Zhu, *Energy Fuels*, 2021, **35**, 17353–17371.
35 S. C. Ashok, A. Vazhayil, R. Vinaykumar, J. Thomas, A. A. Jeffery, I. Hasan, N. Thomas, A. K. Yadav and Y. H. Ahn, *J. Energy Storage*, 2024, **86**, 111145.
36 Z. Zhang, X. Ren, C. Luo, G. Wang, Y. Miao, C. Xu and H. Chen, *Int. J. Hydrogen Energy*, 2025, **103**, 12–22.
37 S. Sitole, M. P. Bilibana and N. Ross, *J. Comput. Sci.*, 2025, **9**, 1–32.
38 R. S. Desai, V. S. Jadhav, P. J. Morankar, S. B. Patil, S. B. Sadale, S. R. Pardeshi, D. D. Lad, P. S. Patil, C. W. Jeon and D. S. Dalavi, *J. Electroanal. Chem.*, 2025, **976**, 118800.
39 R. A. A. Nishara and B. M. Parthibavarman, *Ionics*, 2025, DOI: **10.1007/s11581-025-06241-0**.
40 Y. Cao, J. Liang, X. Li, L. Yue, Q. Liu, S. Lu, A. M. Asiri, J. Hu, Y. Luo and X. Sun, *Chem. Commun.*, 2021, **57**, 2343–2355.
41 J. Zhang, K. A. S. Usman, M. A. N. Judicpa, D. Hegh, P. A. Lynch and J. M. Razal, *Small Methods*, 2023, **7**, 1–16.
42 M. Mahmood, A. Rasheed, I. Ayman, T. Rasheed, S. Munir, S. Ajmal, P. O. Agboola, M. F. Warsi and M. Shahid, *Energy Fuels*, 2021, **35**, 3469–3478.
43 J. Pani, P. Chaudhary, H. Borkar and M. F. Lin, *J. Mater. Chem. A*, 2025, DOI: **10.1039/d4ta05816j**.
44 X. Xiao, G. Wang, M. Zhang, Z. Wang, R. Zhao and Y. Wang, *Ionics*, 2018, **24**, 2435–2443.
45 S. Zhao, Q. Li, F. Li and Z. Liang, *J. Sol-Gel Sci. Technol.*, 2017, **81**, 544–555.
46 D. Maru, J. Pani, H. Borkar and V. S. Palaparthy, *ACS Appl. Electron. Mater.*, 2024, DOI: **10.1021/acsaelm.3c01348**.
47 Y. Li, X. Zhou, J. Wang, Q. Deng, M. Li, S. Du, Y. H. Han, J. Lee and Q. Huang, *RSC Adv.*, 2017, **7**, 24698–24708.
48 R. H. Althomali, E. A. M. Saleh, R. S. Bhat, S. Askar, I. B. Sapaev, M. A. A. Najm, B. M. Ridha, A. H. Alsalamy and R. Riyadh, *Opt. Mater.*, 2023, **143**, 114248.
49 W. Wang, *J. Mater. Sci. Mater. Electron.*, 2021, **32**, 16662–16668.
50 W. Y. Chen, X. Jiang, S. N. Lai, D. Peroulis and L. Stanciu, *Nat. Commun.*, 2020, **11**, 1–10.
51 A. M. Jastrzębska, A. Szuplewska, A. Rozmysłowska-Wojciechowska, M. Chudy, A. Olszyna, M. Birowska, M. Popielski, J. A. Majewski, B. Scheibe, V. Natu and M. W. Barsoum, *2D Mater.*, 2020, DOI: **10.1088/2053-1583/ab6a60**.
52 M. Y. Kim, M. H. Naveen, N. G. Gurudatt and Y. B. Shim, *Small*, 2017, DOI: **10.1002/smll.201700502**.
53 M. Yu, Z. Feng, Y. Huang, K. Wang and L. Liu, *J. Mater. Sci. Mater. Electron.*, 2019, **30**, 4174–4183.
54 G. P. Kamble, A. A. Kashale, S. S. Kolekar, I. P. Chen and B. R. Sathe, *J. Mater. Sci. Mater. Electron.*, 2021, **32**, 5859–5869.
55 X. Niu, Y. Chen and H. Hu, *Membranes*, 2022, **12**, 4–13.

56 R. Wang, Y. Wang, C. Wu, T. Zhai, J. Yang, B. Sun, S. Duhm and N. Koch, *Adv. Funct. Mater.*, 2019, DOI: **10.1002/adfm.201903440**.
57 Q. Wang, Z. Zhang, Z. Zhang, X. Zhou and G. Ma, *J. Solid State Electrochem.*, 2019, **23**, 361–365.
58 M. S. Javed, H. Lei, H. U. Shah, S. Asim, R. Raza and W. Mai, *J. Mater. Chem. A*, 2019, **7**, 24543–24556.
59 M. Pathak, P. Mane, B. Chakraborty and C. S. Rout, *J. Energy Storage*, 2023, **66**, 107475.
60 M. Pathak, S. R. Polaki and C. S. Rout, *RSC Adv.*, 2022, **12**, 10788–10799.
61 J. Pani and H. Borkar, *J. Electroanal. Chem.*, 2024, **956**, 118092.
62 M. Dahlqvist, M. W. Barsoum and J. Rosen, *Mater. Today*, 2024, **72**, 1–24.